inorganics

MDPI

Article

The 1D Hybrid Material Allylimidazolium Iodoantimonate: A Combined Experimental and Theoretical Study

Hela Ferjani [1], Rim Bechaieb [2], Diego M. Gil [3] and Axel Klein [4,*]

[1] Center for Innovation and Entrepreneurship, Imam Mohammad Ibn Saud Islamic University (IMSIU), Riyadh 11623, Saudi Arabia; hhferjani@imamu.edu.sa
[2] Laboratoire de Chimie Théorique, Sorbonne Universités, UPMC Univ Paris 06, UMR 7616, F-75005 Paris, France; rim.bechaieb@gmail.com
[3] INBIOFAL (CONICET-UNT), Instituto de Química Orgánica, Facultad de Bioquímica, Química y Farmacia, Universidad Nacional de Tucumán, Ayacucho 471, San Miguel de Tucumán T4000INI, Argentina; diego.gil@fbqf.unt.edu.ar
[4] Institute for Inorganic and Materials Chemistry, Department of Chemistry and Biochemistry, Faculty of Mathematics and Natural Sciences, University of Cologne, Greinstrasse 6, 50939 Köln, Germany
* Correspondence: axel.klein@uni-koeln.de

Abstract

The one-dimensional (1D) Sb(III)-based organic–inorganic hybrid perovskite $(AImd)_2{}^1{}_\infty[SbI_5]$ (AImd = 1-allylimidazolium) crystallizes in the orthorhombic, centrosymmetric space group *P*nma. The structure consists of corner-sharing $[SbI_6]$ octahedra forming 1D chains separated by allylimidazolium cations. Void analysis through Mercury CSD software confirmed a densely packed lattice with a calculated void volume of 1.1%. Integrated quantum theory of atoms in molecules (QTAIM) and non-covalent interactions index (NCI) analyses showed that C–H···I interactions between the cations and the $^1{}_\infty[SbI_5]^{2-}$ network predominantly stabilize the supramolecular assembly followed by N–H···I hydrogen bonds. The calculated growth morphology (GM) model fits very well to the experimental morphology. UV–Vis diffuse reflectance spectroscopy allowed us to determine the optical band gap to 3.15 eV. Density functional theory (DFT) calculations employing the B3LYP, CAM-B3LYP, and PBE0 functionals were benchmarked against experimental data. CAM-B3LYP best reproduced Sb–I bond lengths, while PBE0 more accurately captured the HOMO–LUMO gap and the associated electronic descriptors. These results support the assignment of an inorganic-to-organic [Sb–I] → π* charge-transfer excitation, and clarify how structural dimensionality and cation identity shape the material's optoelectronic properties.

Keywords: iodoantimonate(III); one-dimensional hybrid perovskite; X-ray diffraction; morphology; QTAIM; NCI; DFT benchmarking

Academic Editor: Chiara Dionigi

Received: 30 May 2025
Revised: 11 July 2025
Accepted: 11 July 2025
Published: 15 July 2025

Citation: Ferjani, H.; Bechaieb, R.; Gil, D.M.; Klein, A. The 1D Hybrid Material Allylimidazolium Iodoantimonate: A Combined Experimental and Theoretical Study. *Inorganics* **2025**, *13*, 243. https://doi.org/10.3390/inorganics13070243

1. Introduction

Over the past two decades, extensive research has been devoted to the so-called organic–inorganic hybrid perovskites, generally represented by the formula $(A)_a[M_bX_c]$, where A is an organic cation, M is a divalent or trivalent metal, and X represents a halide or chalcogenide. The high interest in these materials is due to their interesting photophysical (photo semiconducting) and photochemical properties allowing their applications in photovoltaics or photocatalysis [1–9]. These materials combine many of the favorable attributes of traditional inorganic semiconductors such as high charge carrier mobility and strong absorption coefficients, with the processability and structural versatility of organic components [8,10–12]. Lead halide perovskites with the prototypical

$(MeNH_3)PbI_3$ as light harvesters have revolutionized the field of photovoltaics, achieving unprecedented power conversion efficiencies and eventually driving the development towards commercialization [13,14]. However, despite their popularity, lead- and tin-based hybrid materials pose challenges related to chemical instability and toxicity [3,15–20].

As a result, alternative systems incorporating less toxic metals have gained increasing attention, in particular halide structures based on the p-block elements Sb and Bi [18,19,21–29]. While Bi(III) halide compounds have been studied extensively, their Sb(III) counterparts remain relatively underexplored. The main reason is that the $6s^2$ electronic configuration of Bi(III) is considered to be superior to $5s^2$ Sb(III) in providing the necessary electronic structure [28,29]. Nonetheless, Sb(III)-based perovskite-like materials are emerging as promising candidates for photovoltaic and photocatalytic applications due to their low toxicity and their good structural stability [25–27,30–50].

Structurally, the Sb(III)-based perovskites feature in most of the cases distorted $[SbX_6]^{n-}$ octahedra which are interconnected through their corners, edges, or faces to 1D, 2D, or 3D structures [25,27,29–38]. Exceptional cases feature pseudo-octahedral pentacoordinate $[SbCl_5]^{2-}$ with a stereochemically active $5s^2$ lone pair [39,40]. The $[SbX_6]^{n-}$ octahedra might well occur as isolated monomeric units, or edge- or face-sharing dimeric, or oligomeric units. These materials are frequently called zero-dimensional (0D) [41–51]. Crystal packing in the low-dimensional hybrid materials is characterized by a combination of the covalent anionic halidometalate structure with the electrostatic forces connecting the organic cations to the anionic scaffold. These forces are frequently augmented with further non-covalent interactions such as hydrogen bonding, halogen bonding, and van der Waals interactions, and are, thus, mostly driven by the nature of the organic cation, particularly its size, shape, functional groups, charge, and steric effects [31,32,37,41,43–47,49–51].

Herein, we report the synthesis and characterization of a new 1D antimony iodide hybrid compound, $(AImd)_2{}^1{}_\infty[SbI_5]$, containing the allylimidazolium cation ($AImd^+$) (Scheme 1). Single-crystal X-ray diffraction shows ${}^1{}_\infty[SbI_5]^{2-}$ chains of *cis*-corner-sharing $[SbI_6]^{3-}$ octahedra separated by the organic cations. Crystal morphology predictions were carried out describing the chemical groups present on dominant crystal faces and their influence on face growth. The optical properties were investigated using UV–vis absorption and diffuse reflectance spectroscopy. Density Functional Theory (DFT) calculations, benchmarking the B3LYP, CAM-B3LYP, and PBE0 functionals and including long-range corrections, were carried out to gain further insight into the electronic structure.

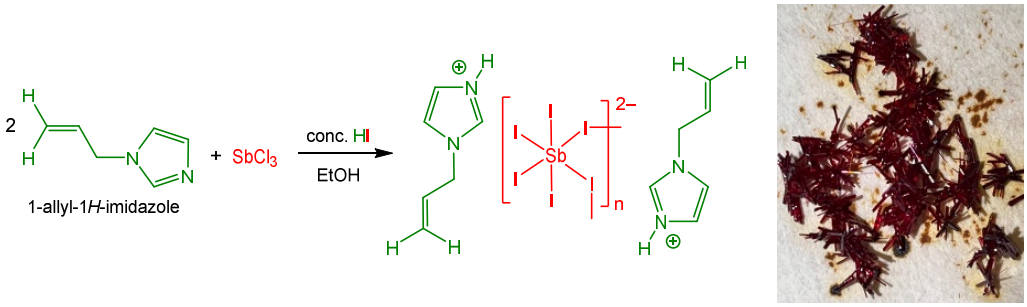

Scheme 1. Synthesis of the title structure $(AImd)_2{}^1{}_\infty[SbI_5]$ (AImd = allylimidazolium) (**left**) and a photograph of the red crystals (**right**).

2. Results and Discussion

2.1. Single-Crystal X-Ray Structure Determination

The red compound $(AImd)_2{}^1{}_\infty[SbI_5]$ (AImd = allylimidazolium) crystallizes in the orthorhombic, centrosymmetric space group *P*nma (No. 62) (structure solution and refinement data in Table S1, Supplementary Materials). The structure consists of anionic

$^1{}_\infty[SbI_5]^{2-}$ chains and allylimidazolium cations. The anionic framework is composed of *cis*-zigzag $^1{}_\infty[SbI_5]^{2-}$ chains formed through corner-sharing, distorted $[SbI_6]$ octahedra. Each Sb(III) center adopts a six-coordinate geometry (Figure 1), with Sb–I bond lengths ranging from 2.855(1) Å to 3.308(1) Å (Table 1), consistent with previously reported iodoantimonate structures [30–33,35,38]. The anionic chains align parallel to each other along the crystallographic *a* axis, forming well-separated chains of $[SbI_5]^{2-}$ units. The interchain I···I distance of 4.299 Å exceeds the sum of the van der Waals radii for iodine (3.96 Å), indicating the absence of halogen bonding and minimal electronic interaction between adjacent chains [52].

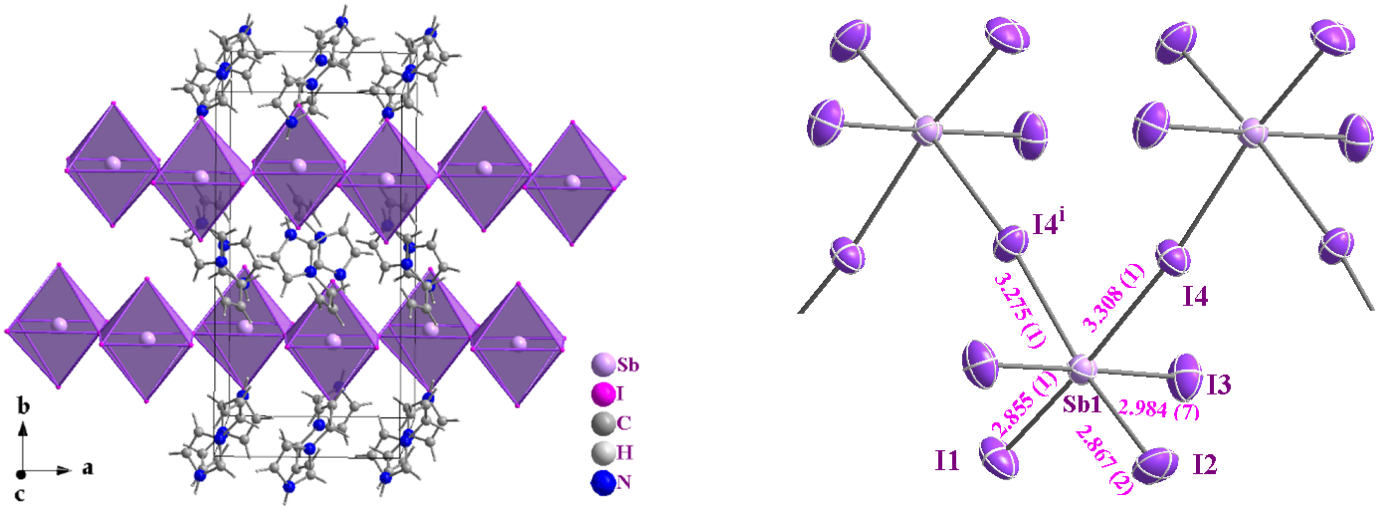

Figure 1. Perspective view on the crystal structure of $(AImd)_2{}^1{}_\infty[SbI_5]$ showing the chains of *cis* corner-sharing $[BiI_6]^{3-}$ octahedra (in purple (**left**)) and a view on the zig-zag $^1{}_\infty[SbI_5]^{2-}$ chain with atom numbering and selected distances in Å (**right**).

Table 1. Selected experimental geometric parameters of $(AImd)_2{}^1{}_\infty[SbI_5]$.

Bond lengths (Å)		Sb1–I3	2.984(8)
Sb1–I1	2.855(1)	Sb1–I3^i	2.984(8)
Sb1–I2	2.867(1)	Sb1–I4	3.308(1)
Bond angles (°)			
I1–Sb1–I2	98.89(5)	I3–Sb1–I3^i	178.70(5)
I1–Sb1–I3	89.87(2)	I1–Sb1–I4	175.89(5)
I2–Sb1–I3	89.39(2)	I2–Sb1–I4	85.23(4)
I1–Sb1–I3^i	89.87(2)	I3–Sb1–I4	90.17(2)
I2–Sb1–I3^i	89.39(2)	I3^i–Sb1–I4	90.17(2)

Symmetry code: i = x, $-y + 1/2$, z. More data are shown in Table S2.

The shorter Sb–I bonds (2.855(1)–2.984(7) Å) correspond to the terminal iodide ligands I1 to I3, while the longer bonds of 3.308 Å and 3.275(1) involve the bridging iodides I4 and I4^i (i = x, –y + 1/2, z) (Figure 1 and Table 1). The slight difference in bond lengths between Sb1–I4 and Sb1–I4^i (0.033 Å) is attributed to hydrogen bonding involving the I4 atom. The Sb1–I4–Sb1 bond angle is approximately 172.9°, supporting the idea that I4 is slightly displaced under the influence of N2–H2A···I4 hydrogen bonding with the cation (Figure 2a and Table 2).

The $AImd^+$ cations were refined with positional disorder on the atoms C4, C5, and C6 and with an intramolecular C6–H···N1 hydrogen bond of about 2.47 Å (Figure 2b). The same distortion and geometry have been observed in the 1D $(AImd)_2{}^1{}_\infty[BiCl_5]$ (centrosymmetric space group $C2/c$) [53] and the 0D $(AImd)_2[SnCl_6]$ (space group $P2_1/n$) [54]. The

cations occupy the space between the anionic chains and contribute through coulombic forces, but also through a network of weak hydrogen bonding interactions, in particular N–H···I and C–H···I (see Figure 2 and Table 2), with the $^1_\infty[SbI_5]^{2-}$ scaffold to the overall structural stability. In turn, the hydrogen bonds induce subtle distortions in the $^1_\infty[SbI_5]^{2-}$ chain. No significant π–π stacking interactions are observed, in contrast to related imidazolium-based systems [53–55].

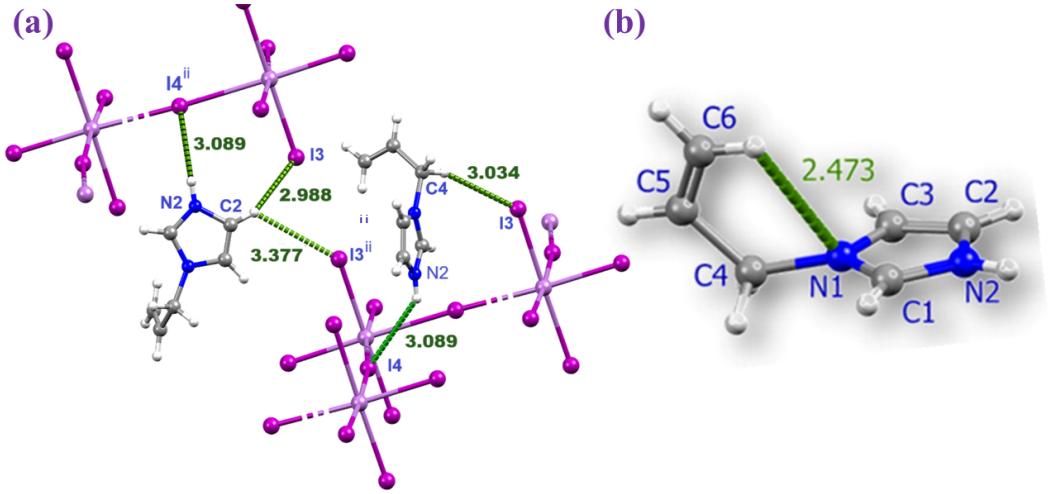

Figure 2. Magnified view of the hydrogen bonding between the AImd$^+$ cations and the inorganic chain in (AImd)$_2$ $^1_\infty[SbI_5]$ (**a**) and the intramolecular hydrogen bonding in AImd$^+$ (**b**).

Table 2. Hydrogen bond geometries in (AImd)$_2$ $^1_\infty[SbI_5]$.

unit	distances (Å)			angles (°)
D–H···*A*	*D*–H	H···*A*	*D*···*A*	*D*–H···*A*
N2–H2*A*···I4 ^{ii}	0.86	3.09	3.78(1)	141
C4–H4*A*···I3 ^{iii}	0.97	3.03	3.91(3)	152
C2–H2···I3 ^{ii}	0.93	2.99	3.73(2)	138
C1–H1···I4 ^{iv}	0.93	3.17	3.93(2)	141

Symmetry codes: (ii) $x + 1, y + 1, z$; (iii) $x, y + 1, z$; (iv) $x + 1/2, y + 1, -z + 1/2$.

The observed bond lengths and angles in the $^1_\infty[SbI_5]^{2-}$ scaffold are consistent with those in the related 1D corner-sharing iodoantimonates (A)$_n$ $^1_\infty[SbI_5]$ (n = 1 or 2) with the cations 2-methyl-1,5-pentanediammonium (2-MPDA^{2+}) [35], *N*,*N*,*N*′-trimethylethylenediammonium (TMEDA^{2+}) [33], *S*-Me-thiouronium ($CH_3SC(NH_2)_2$) [38], and the chiral (*R*)-(+)-α-ethylbenzylammonium [32], but also with those in the edge-sharing (C_7H_7[SbI_4] (C_7H_7 = tropylium) [34].

Quite recently, the use of methylhydrazinium cations gave two polymorphs, of which one strongly resembles our (AImd)$_2$ $^1_\infty[SbI_5]$ structure, while the other contains the corner-sharing dimers $[Sb_2I_{11}]^{2-}$ [30]. The use of piperazinium derivatives (RPip$^+$) as cation allowed us to obtain $^1_\infty[SbI_4]^{2-}$ containing structures with edge-sharing [SbI_6] octahedra, such as (RPip)[SbI_4]$_2$·4H_2O, (RPip)[SbI_4]$_2$·3H_2O, and two polymorphs of (RPip)[SbI_4]$_2$·2H_2O, but also the 0D tetrameric (RPip)[Sb_4I_{16}]0.5·H_2O [41]. Furthermore, the use of (*S*)-1-phenylethylammonium gave a structure containing edge-sharing $Sb_2I_{10}^{4-}$ dimers [41]. Only small structural variations in a series of dimeric oxonium cations, including dimethyl formamide (DMFH·DMF$^+$), dimethylacetamide (DMAH·DMA$^+$), 2-pyrrolidon (2-PyrrH·2-Pyrr$^+$), and *N*-Methyl-2-pyrrolidon (NMPH·NMP$^+$), led to various 0D structural motives, including face-sharing dimers (DMFH·DMF)$_2Sb_2I_9$ and (DMAH·DMA)$_2Sb_2I_9$, edge-sharing tetramers (2-PyrrH·2-Pyrr)$_2Sb_2I_8$, and trinuclear

$(NMPH{\cdot}NMP)_3Sb_3I_{12}$ [36]. Thus, prediction of the formed compounds based on the cations remains challenging.

To further quantify the degree of distortion in the $[SbI_6]$ octahedra, we employed the distortion index (Δd) and bond angle variance (σ) derived from Equations (1) and (2) [56].

$$\Delta_d = \frac{1}{n}\sum_{i=1}^{n}\left(\frac{d_i - d_{av}}{d_{av}}\right)^2 \quad (1)$$

$$\sigma^2 = \frac{1}{n}\sum_{i=1}^{n}(\theta_i - \theta_0)^2 \quad (2)$$

where d_i represents each individual Sb–I bond length, d_{av} is the average bond length, θ_i represents the i^{th} I–Sb–I bond angle within each octahedral unit, and θ_0 is 90° (or 180° for linear angles). Larger values for the distortion index (Δd) and bond angle variance (σ^2) indicate enhanced distortion.

For $(AImd)_2{}^1{}_\infty[SbI_5]$, the distortion index ($\Delta d$) is 0.0055, and the bond angle variance (σ^2) is $(12.12°)^2$, confirming significant distortion, particularly in bond angles, primarily due to hydrogen bonding and the stereochemical influence of the $5s^2$ lone pair on Sb(III).

A comparison of octahedral distortion values in numerous 1D Sb–I materials (Table 3) show the structural sensitivity to hydrogen bonding and Sb(III) lone pair stereochemistry. The $(AImd)_2{}^1{}_\infty[SbI_5]$ structure has a moderate distortion index similar to the $(2\text{-}MPDA)^1{}_\infty[SbI_5]$ compound (σ^2 = 12.56) and similar I4 displacement due to strong H···I hydrogen bonding interactions. $(TMEDA)^1{}_\infty[SbI_5]$ exhibits lesser distortion (Δ_{oct} = 0.0015; σ^2 = 8.992), indicating minor structural disruption from weaker hydrogen bonding and more influence from the stereochemically active $5s^2$ lone pair. $(CH_3SC(NH_2)_2)^1{}_\infty[SbI_5]$ and $(R\text{-}EBAH)_2{}^1{}_\infty[SbI_5]$ exhibit different characteristics. The former has intermediate distortions with hydrogen bonding affecting I1, while the latter has the largest Δ_{oct} (0.0659) and σ^2 (18.746), indicating a significant divergence from ideal octahedral geometry. This investigation suggests that even little changes in cation type and hydrogen bonding ability can significantly influence $[SbI_6]$ octahedral geometry and impact structural predictability in Sb(III) iodide frameworks [32,35].

Table 3. Octahedral distortion parameters for $(AImd)_2{}^1{}_\infty[SbI_5]$ and selected reported 1D Sb–I materials.

compound	Δ_{oct}	$\sigma_{oct}{}^2$	long Sb–I bond (Å)	d(H···I) Å	effect on structure	Ref.
$(AImd)_2{}^1{}_\infty[SbI_5]$	0.0055	12.12	3.308 (1)	3.09	I4 displaced due to hydrogen bonding	This work
$(2\text{-}MPDA)^1{}_\infty[SbI_5]$	0.0026	12.56	3.210 (1)	2.93	I4 displaced due to hydrogen bonding	[35]
$(TMEDA)^1{}_\infty[SbI_5]$	0.0015	8.992	3.199 (9)	-	stereoactivity of $5s^2$ lone pair	[33]
$(CH_3SC(NH_2)_2)^1{}_\infty[SbI_5]$	0.0039	7.51	3.344 (3)	2.94	I1 displaced due to hydrogen bonding	[38]
$(R\text{-}EBAH)_2{}^1{}_\infty[SbI_5]$	0.0659	18.746	3.255 (2)	2.88	I4 displaced due to hydrogen bonding	[32]

2.2. DFT Geometry Optimization

In DFT geometry optimization using a simplified model consisting of one $AImd^+$ cation and one $[SbI_4]^-$ anion for the benchmarking of the three functionals B3LYP, CAM-B3LYP, and PBE0, combined with LANL2DZ or SDD basis sets, CAM-B3LYP gave the best agreement with the experimental data (Table 4), particularly for the Sb–I interactions that define the $^1{}_\infty[SbI_5]^{2-}$ scaffold. Notably, the CAM-B3LYP/LANL2DZ combination reproduced the longest Sb–I bond (Sb1–I4) within 0.03 Å of the experimental value, underscoring the importance of including long-range exchange and relativistic corrections in systems dominated by heavy atoms and dispersive interactions, in agreement with similar studies [36,41,46,57]. While all functionals slightly overestimate the C–N and C–C bond

lengths, likely due to limitations in ECP basis sets for lighter atoms, CAM-B3LYP performs consistently across both heavy and light atoms. This is further supported by RMSD analysis (Figure 3) quantifying the deviation between DFT-calculated and experimental geometries, confirming the superior performance of CAM-B3LYP.

Table 4. Selected experimental and DFT-calculated equilibrium geometry parameters for $(AImd)_2{}^1{}_\infty[SbI_5]$ [a].

	Exp	B3LYP/ LANL2DZ	B3LYP/ SDD	CAM/ LANL2DZ	CAM/ SDD	PBE0/ LANL2DZ	PBE0/ SDD
Sb1–I1	2.855(1)	2.92342	2.89780	2.88125	2.87243	2.89065	2.88086
Sb1–I2	2.867(1)	2.91104	2.91454	2.87727	2.86559	2.88333	2.87032
Sb1–I3	2.984(1)	2.96581	2.95290	2.94494	2.93347	2.94718	2.93301
Sb1–I4	3.308(1)	3.24489	3.23021	3.27784	3.27024	3.22004	3.21026
C1–N2	1.27(3)	1.33650	1.32956	1.32262	1.32247	1.32407	1.32384
C1–N1	1.32(2)	1.32961	1.33653	1.32984	1.32999	1.33121	1.33136
C2–C3	1.22(3)	1.36100	1.36107	1.35441	1.35447	1.35886	1.35890
C2–N2	1.40(3)	1.37680	1.37685	1.37228	1.37226	1.36888	1.36887

[a] Calculated for a model consisting of one $AImd^+$ cation and one $[SbI_4]^-$ anion.

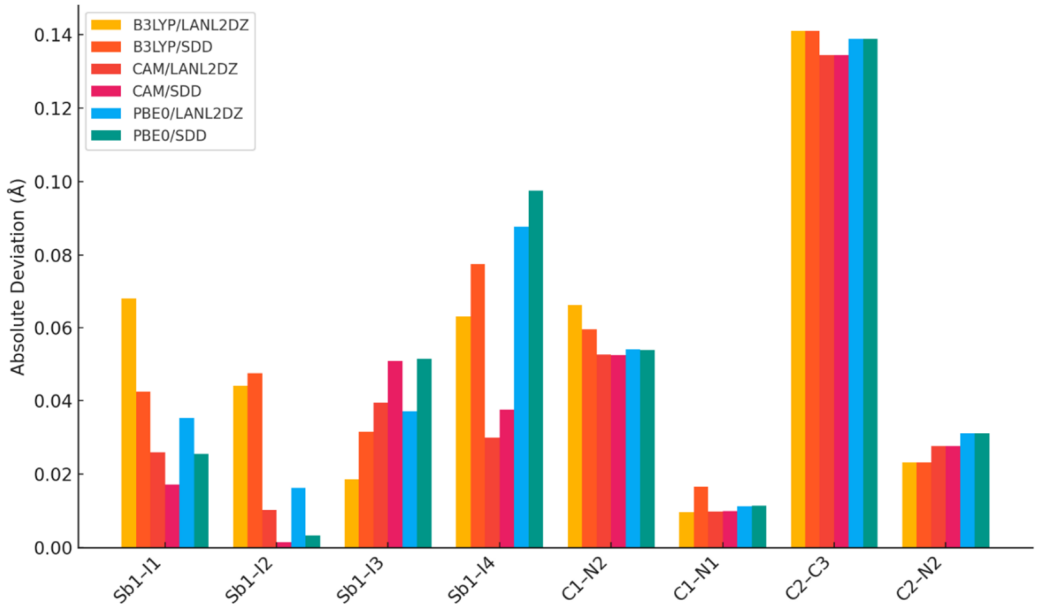

Figure 3. Root-mean-square deviation (RMSD) calculation between experimental and theoretical equilibrium distance.

2.3. Computational Characterization of Non-Covalent Interactions

The N–H···I and C–H···I hydrogen bonds found in the crystal structure were further analyzed using the quantum theory of atoms in molecules (QTAIM) and the non-covalent interactions index (NCI) using a monomeric $(AImd)_2[SbI_5\cdots I]$ model that includes two $AImd^+$ cations and an $[SbI_5\cdots I]^{2-}$ anion (Figure 4). The NCI allows the visualization of interactions in real space and the determination of their attractive or repulsive nature.

The calculated interaction energy $\Delta E = -193.1$ kcal/mol between the two organic $AImd^+$ cations and the $[SbI_5\cdots I]^{2-}$ dianion in the model represents a strong coulombic attraction.

The bifurcated N2–H2A···I4 and N2–H2A···I2 hydrogen bonds are characterized by two bond critical points (BCPs) and bond paths connecting the N2–H2A function of the imidazolium with both the I4 and I3 atoms (**a** and **b** in Figure 4b). These interactions are associated with small green isosurfaces in the NCI plot, indicating medium to weak contributions from these hydrogen bonds to the total energy.

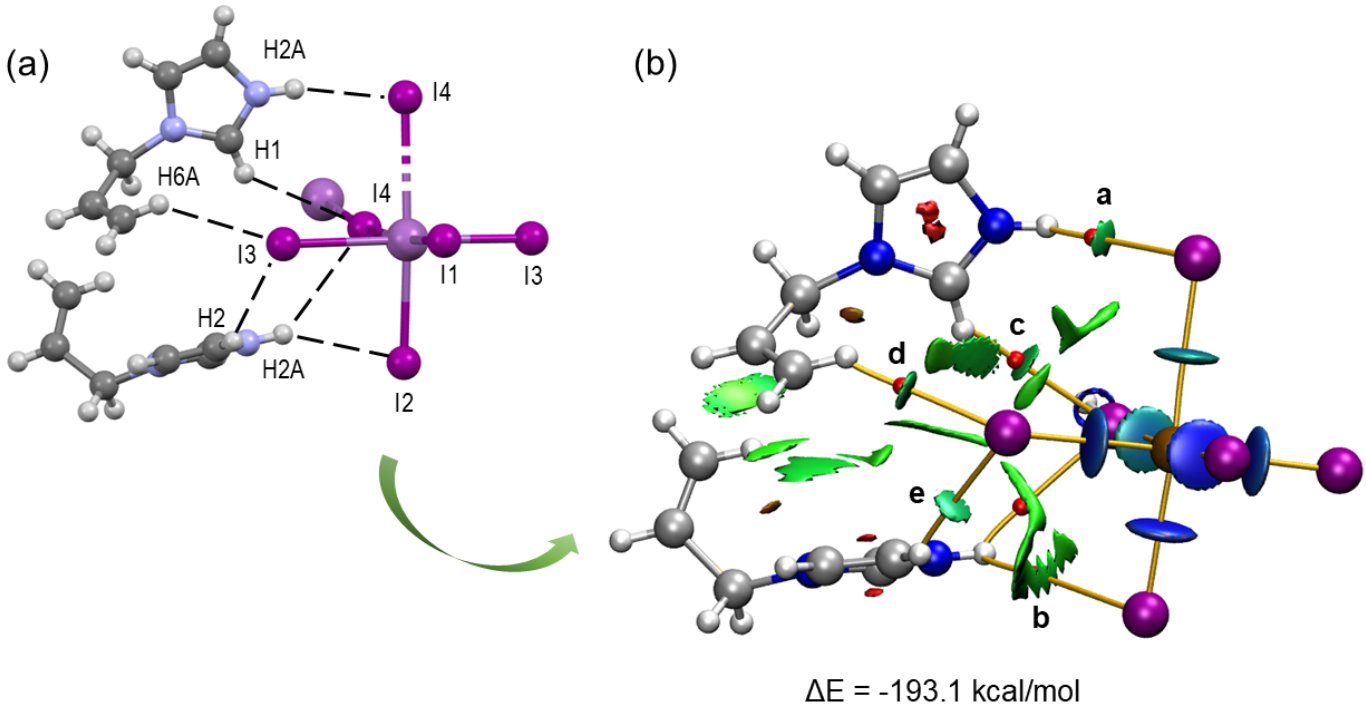

Figure 4. (**a**) View of the non-covalent interactions in the X-ray structure of $(AImd)_2{}^1{}_\infty[SbI_5]$ with the hydrogen bonds shown as dashed lines. (**b**) Combined QTAIM (bond CP in red, bond paths as orange lines) and NCI (green isosurfaces representing hydrogen bonding) plot of an $(AImd)_2[SbI_5\cdots I]$ model.

The strength of the hydrogen bonds was further evaluated using the potential energy density $V(r)$ at the bond critical points [58]. The contributions of the N2–H2A···I4 and N2–H2A···I2 hydrogen bonds are −1.004 and −0.345 kcal/mol, respectively (Table S4). The C–H···I interactions involving the I3 and I4 atoms of the $[SbI_5]^{2-}$ anions and the H1 and H6A atoms of the organic cations reveal three BCPs (points **c**, **d**, and **e** in Figure 4b), bond paths, and green NCI plot isosurfaces, indicating moderate to weak interaction. With −1.067 and −1.381 kcal/mol for C6–H6A···I3 and C2–H2···I3, respectively, they are markedly stronger than the N–H···I interactions. These results confirm the reliability of the hydrogen bond energy predictor based on the potential energy density [$V(r)$]. This methodology was previously validated in similar studies [59,60].

2.4. Crystal Habitus Simulation and Crystal Face Indexing

The crystal morphology of $(AImd)_2{}^1{}_\infty[SbI_5]$ was examined using the Bravais–Friedel–Donnay–Harker (BFDH) approach along with the more energetically comprehensive growth morphology (GM) model (Figure 5). Table 5 outlines key features of the crystal structure and compares the two morphology prediction methods based on the percentage of total facet area and calculated total attachment energy E_{att} (total).

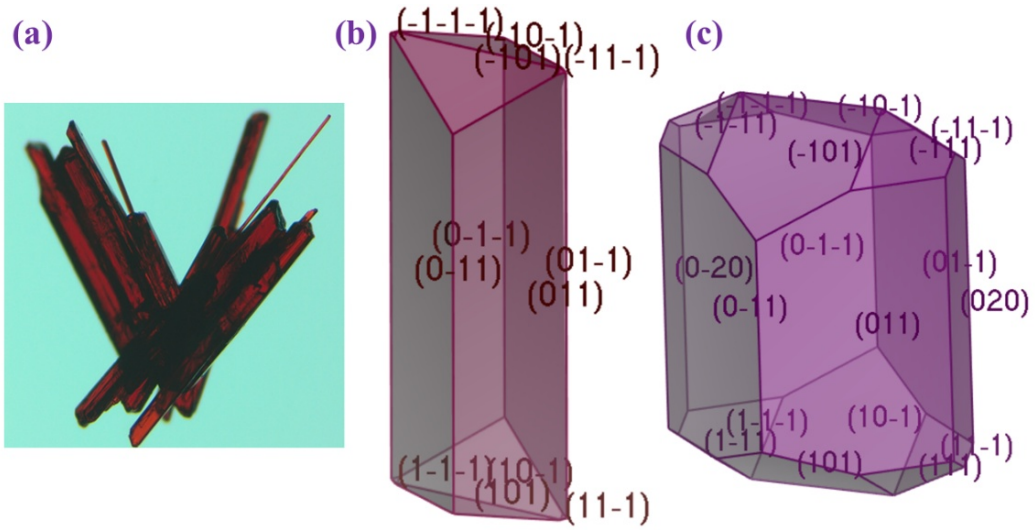

Figure 5. (**a**) Experimental habit of $(AImd)_2{}^1{}_\infty[SbI_5]$ and DFT-calculated habit using the (**b**) GM model and (**c**) BFDH model.

Table 5. Calculated main morphology faces of $(AImd)_2{}^1{}_\infty[SbI_5]$ [a].

experimental			models		
			BFDH	GM	
h k l	multiplicity	d_{hkl} (Å)	% total facet area	E_{att} (total) (kcal·mol^{-1})	% total facet area
(0 1 1)	4	11.51	57.70	−14.73	88.63
(1 0 1)	4	7.75	22.32	−62.42	11.31
(1 1 1)	8	7.11	11.55	−65.72	0.06
(0 2 0)	2	8.92	8.43	–	–

[a] BFDH: Bravais–Friedel–Donnay–Harker model. GM: Growth morphology model. d_{hkl} is the interplanar spacing between lattice planes with (h k l) miller indices. % of the total facet area is determined by the formula 100 × (hkl facet area)/(total surface area). E_{att} (total) is the total attachment energy.

The $(AImd)_2{}^1{}_\infty[SbI_5]$ crystals show a longitudinal blade-like shape (Figure 5a). This morphology is best reproduced by the GM model (Figure 5b), while the BFDH model predicts a truncated block, overestimating contributions from minor facets (Figure 5c). While GM incorporates the attachment energy (E_{att}) and surface energetics allowing growth prediction, BFDH calculates a structure model in the gas phase and neglects intermolecular interactions and energetic considerations, which might explain the poorer prediction using the BFDH model.

Following the GM model, the lateral (0 1 1) face is the most prominent, accounting for 88.63% of the total surface area (Table 5). This face grows slowly due to its low attachment energy of about −15 kcal·mol^{-1}. In contrast, the (1 0 1) and (1 1 1) facets, which exhibit significantly higher attachment energies of over 60 kcal·mol^{-1}, contribute far less to the overall morphology (11.31% and 0.06%), but grow much faster.

The dominant (0 1 1) face exhibits the highest concentration of polar functional groups, including N–H donors and exposed iodide ions (Figure 6), making it the most likely surface for intermolecular interactions, adsorption, or reactivity. This finding is consistent with the Hartman–Perdok theory [61], which asserts that crystal faces exhibiting robust, directed intermolecular contacts have slower growth and, thus, predominate the crystal habit. The abundance of hydrogen bonding and electrostatic interactions on the (0 1 1) face increases its thermodynamic stability and restricts its growth rate, hence strengthening its morphological importance.

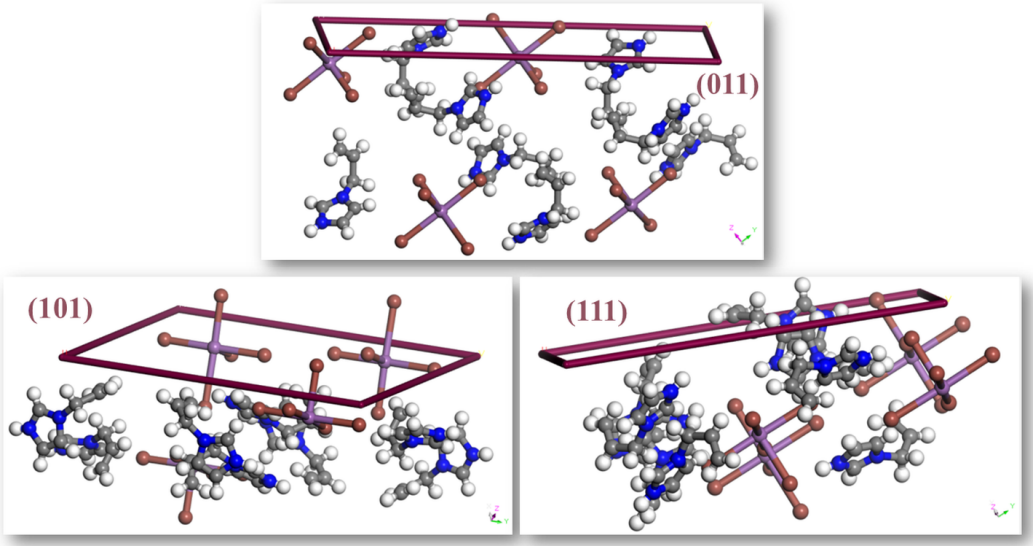

Figure 6. Morphologically significant faces in $(AImd)_2{}^1{}_\infty[SbI_5]$ with Miller indices.

2.5. Void Analysis

Void analysis of the title compound reveals the presence of minor voids within the unit cell (void volume ~27.39 Å^3), accounting for approximately 1.1% of the total unit cell volume. This corresponds to a relatively compact and densely packed structure with minimal interstitial space (highlighted by brown and yellow surfaces in Figure S5). These voids are likely the result of slight packing inefficiencies between the organic and inorganic components.

Void analysis data, summarized in Table S2, show a pore-limiting diameter of 1.25 Å. The one-dimensional percolation pathway suggests that any diffusion or transport within the pore network is likely to be highly anisotropic and confined to narrow channels. The total helium-accessible surface area is virtually zero, indicating that although small voids are present, they are not sufficiently interconnected. This further implies low permeability of the material, along with enhanced structural stability and hardness attributes that may be beneficial for optoelectronic applications.

2.6. FT-IR and Raman Spectroscopy

The Fourier-transformed infrared (FT-IR) spectrum of $(AImd)_2{}^1{}_\infty[SbI_5]$ (Figure S6) represents the vibrational modes of the organic cation and closely resembles those of previously reported allylimidazolium-based hybrid compounds [53–55].

The broad weak band observed at ν = 3460 cm^{-1} corresponds to N–H stretching vibrations, while the peaks at 1276 cm^{-1} and 1844 cm^{-1} are attributed to the in-plane and out-of-plane deformations of the N–H bond. The peaks at 3274 and 3114 cm^{-1} represent the C–H stretching vibrations in the imidazole ring. The bands observed at 2983 and 2853 cm^{-1} correspond to the antisymmetric and symmetric stretching vibrations of the C–H bonds in the vinyl moiety. The stretching modes of the vinyl C=C bonds were observed at 1428 cm^{-1}. C–H rocking, twisting, and wagging modes in the vinyl group were found at 1270 cm^{-1}, 1129 cm^{-1}, 1073 cm^{-1}, and 990 cm^{-1}. The bands ranging from 1725 to 1568 cm^{-1} primarily represent the stretching of C=C and C=N bonds within the imidazole ring. The imidazole bending modes are observed at 751 and 615 cm^{-1}. These experimental assignments are further supported by DFT-calculated vibrational frequencies obtained at the CAM-B3LYP/SDD–6-311++G** level. The computed N–H and C–H stretching modes appear in the expected 3100–3450 cm^{-1} region, closely matching the observed bands at 3114, 3274, and 3460 cm^{-1}. Similarly, theoretical values for C=C, C=N, and C–C skeletal vibrations correspond well with experimental bands in the 1400–1750 cm^{-1} range, typically within

20–30 cm^{-1}. The low-frequency region associated with Sb–I stretching and bending modes (below 300 cm^{-1}) is also well reproduced in the calculated spectrum, supporting the structural integrity of the inorganic chain. This good qualitative agreement reinforces the reliability of the mode assignments and highlights the consistency between theory and experiment.

Bands corresponding to Sb–I bonds appear at frequencies below 400 cm^{-1} in the Raman spectrum (Figure S7). The intense Raman band at ν = 156 cm^{-1} is attributed to the symmetric stretching of the *cis*-iodide ligands in keeping with similar structures [36,38]. The band observed at ν = 96 cm^{-1} corresponds to the symmetric vibrations of the bridging iodide groups. A third expected vibrational mode representing the symmetric and asymmetric trans Sb–I groups [36] is absent, likely due to its very low intensity and in line with observations on the structurally very similar 1D material $(CH_3SC(NH_2)_2)_2{}^1{}_\infty[SbI_5]$ [38].

2.7. Optoelectronic Properties

The optical properties of $(AImd)_2{}^1{}_\infty[SbI_5]$ were investigated to evaluate its potential for photovoltaic applications, using solid-state UV–vis absorption and diffuse reflectance spectroscopy (DRS). $(AImd)_2{}^1{}_\infty[SbI_5]$ shows a pronounced absorption edge with an onset at 402 nm (Figure 7), corresponding to an energy of 3.08 eV.

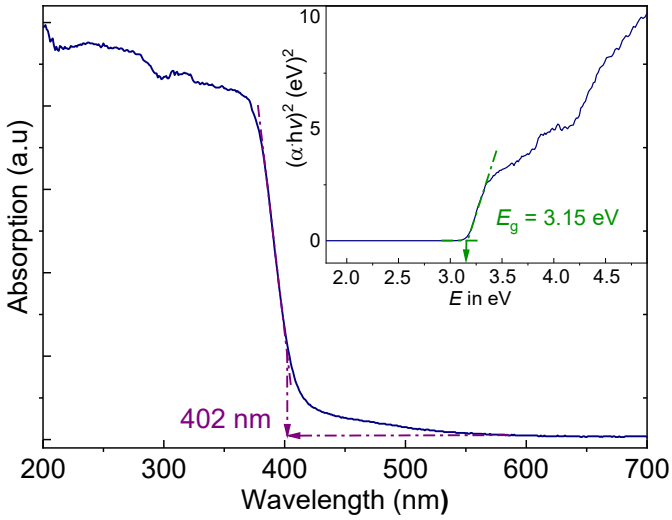

Figure 7. Solid state UV–vis diffuse reflectance spectrum (DRS) of $(AImd)_2{}^1{}_\infty[SbI_5]$. The inset shows the Tauc plot for the calculation of the optical band gap E_g.

The absorption edge is in line with the wine-red color of the crystals. Plotting $(\alpha h\nu)^2$ versus $h\nu$ (Tauc plot) [62] from the Kubelka–Munk function gives an optical band gap of 3.15 eV (Figure 7 inset), which agrees roughly with the absorption edge.

Iodo antimonates often exhibit narrow band gaps around 2 eV, but the values are very strongly dependent on the structures [30,33,37,38,46,48]. For the structurally related corner-sharing 1D two polymorphs of $(MHy)_2{}^1{}_\infty[SbI_5]$, energies of 2.12 and 2.01 eV were reported [30], with 2.01 eV also for $(TMEDA)^1{}_\infty[SbI_5]$ [33], and 1.55 eV for the edge-sharing 1D structure $(C_7H_7)^1{}_\infty[SbI_4]$ [34]. For the structurally related 1D material $(CH_3SC(NH_2)_2)_2{}^1{}_\infty[SbI_5]$, a band gap of 2.41 eV was reported [38], while for $(3A10)[SbI_6]\cdot 3H_2O$ (3A10 = triprotonated 6-amino-5,7-dimethyl-1,3-diazaadamantane) containing isolated $[SbI_6]^{3-}$ ions, a gap energy of 2.5 eV was reported [42]. All these examples underpin that the gap energy strongly depends on the crystal structure. The value for $(AImd)_2{}^1{}_\infty[SbI_5]$ is rather comparable to those of the 0D chlorido antimonate $(PPZ)_2[SbCl_6]\cdot Cl\cdot 5H_2O$ (PPZ = 1-phenylpiperazine; 2.95 eV) [47], the 1D corner-sharing bromido antimonate $(CH_3SC(NH_2)_2)_2{}^1{}_\infty[SbBr_5]$ (3.03 eV) [38], the 1D mixed-halido derivative

$(CH_3SC(NH_2)_2)_2{}^1{}_\infty[SbBr_{1.14}Cl_{3.86}]$ (3.34 eV) [38], or the 1D corner-sharing $(4ApyH)^1{}_\infty[SbI_4]$ (4Apy = 4-aminopyridine) (3.06 eV) [27]. The high band gap energy in $(AImd)_2{}^1{}_\infty[SbI_5]$ can be attributed to limited orbital overlap within the SbI_5 framework. The packing motif and limited interchain contacts likely lead to localized electronic states [37].

Further comparison of similar 1D systems reveals the influence of the organic cation on the optical properties (Table 6). The band gap of $(AImd)_2{}^1{}_\infty[SbI_5]$ exceeds that of $(R\text{-}EBAH)_2{}^1{}_\infty[SbI_5]$ (2.20 eV) [32] and $(2\text{-}MPDA)^1{}_\infty[SbI_5]$ (1.92 eV) [33], highlighting the role of the allylimidazolium cation in modulating the electronic structure. DFT-calculated orbital plots show that the HOMO is localized on the $[SbI_5]^{2-}$ framework while the LUMO resides on the organic π^* system (Figure 8), confirming the limited orbital overlap between chains. This is likely due to weak interchain interactions and restricted π-conjugation in the cation backbone, which together contribute to the increased band gap. A similar trend is observed in the 0D compound $(3A10)[SbI_6]\cdot 3H_2O$, which exhibits a slightly elevated gap of 2.5 eV, consistent with greater electronic isolation. The bismuth analogue, $(AImd)_2{}^1{}_\infty[BiI_5]$, also shows a larger band gap (3.26 eV), confirming that both the metal center and dimensionality significantly influence the optical response. These comparisons underscore the importance of both structural dimensionality and cation identity in tuning the band gap of iodoantimonate materials.

Table 6. Optical band gaps (E_g) of various halide compounds with different structural dimensionalities and cations.

compound	dimensionality	cation	E_g (eV)	Ref
$(AImd)_2{}^1{}_\infty[SbI_5]$	1D	1-allyl-1*H*-imidazolium	3.15	this work
$(R\text{-}EBAH)_2{}^1{}_\infty[SbI_5]$	1D	(*R*)-(+)-α-ethylbenzyl-ammonium	2.20	[32]
$(TMEDA)^1{}_\infty[SbI_5]$	1D	*N*,*N*,*N*′-trimethyl-ethylene-diammonium	2.01	[33]
$(2\text{-}MPDA)^1{}_\infty[SbI_5]$	1D	2-methyl-1,5-pentane-diammonium	1.92	[35]
$(CH_3SC(NH_2)_2)^1{}_\infty[SbI_5]$	1D	$CH_3SC(NH_2)^+$	2.41	[38]
$(3A10)[SbI_6]\cdot 3H_2O$	0D	H_3[6-amino-5,7-dimethyl-1,3-diazaadamantane]$^{3+}$ [a]	2.50	[42]
$(MHy)_2{}^1{}_\infty[SbI_5]$	1D	$[NH_2\text{-}NH_2\text{-}CH_3]^+$	2.12, 2.01 [b]	[30]
$(AImd)_2{}^1{}_\infty[BiCl_5]$	1D	1-allyl-1*H*-imidazolium	3.26	[53]
$(AImd)_2[SnCl_6]$	0D	1-allyl-1*H*-imidazolium	3.72	[54]

[a] Trifold protonated. [b] Two polymorphs.

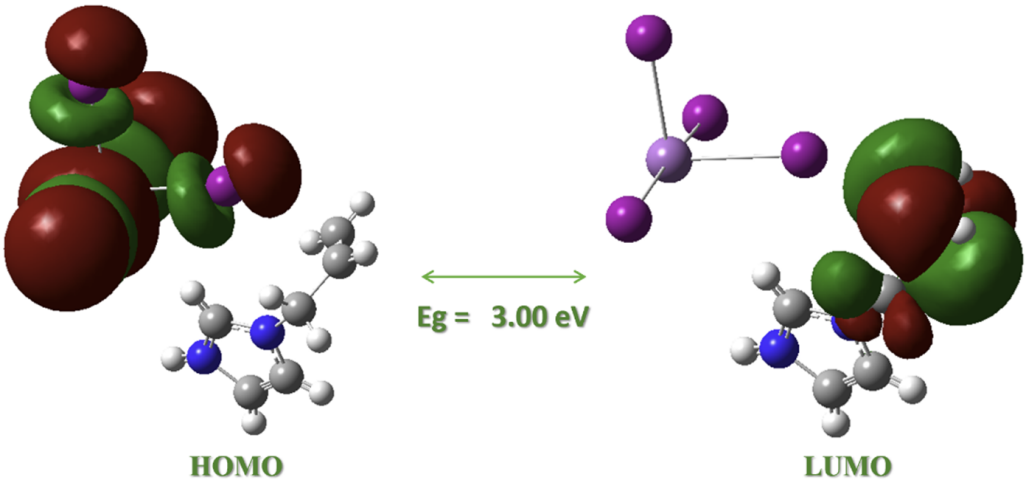

Figure 8. DFT-calculated frontier molecular orbital contributions and energy gap E_g for $(AImd)_2{}^1{}_\infty[SbI_5]$ using the PBE0 functional.

The low-energy electronic transition is provisionally attributed to a charge transfer from the inorganic $^1{}_\infty[SbI_5]^{2-}$ lattice to the π^* orbitals of the organic cation. This has been

previously proposed for $(C_7H_7)^1{}_\infty[SbI_4]$ containing tropylium as organic cation [34]. More frequently, it has been supposed that in such materials a ligand-to-metal charge transfer proceeds from iodine 5p states (forming the main contribution of the valence band) to Sb 5p states (dominating the conduction band) [42,46,48,63,64].

2.8. DFT-Calculated Frontier Orbital Character and Energies

Frontier Molecular Orbitals

Among the tested functionals, CAM-B3LYP provided the best agreement with the experimental bond lengths (see Section 2.2), particularly for the Sb–I interactions. However, when analyzing the electronic structure, PBE0 performed best, yielding a HOMO–LUMO gap of 2.97–3.00 eV (Table 7), in close agreement with the experimentally determined optical gap of 3.15 eV. This observation is consistent with previous studies where PBE0 accurately reproduced band gaps in Sb-based hybrid systems [36,46].

Table 7. DFT-calculated HOMO–LUMO energies for $(AImd)_2{}^1{}_\infty[SbI_5]$ in the crystal.

	B3LYP/ LANL2DZ	B3LYP/ SDD	CAM/ LANL2DZ	CAM/ SDD	PBE0/ LANL2DZ	PBE0/ SDD
E_{HOMO} (eV)	−5.66	−5.73	−6.87	−6.93	−5.94	−5.97
E_{LUMO} (eV)	−3.00	−3.04	−2.13	−2.16	−2.97	−2.96
E_g (eV)	2.66	2.69	4.73	4.77	2.97	3.00

In contrast, B3LYP underestimated the gap (~2.66 eV), and CAM-B3LYP significantly overestimated it (~4.75 eV), reflecting known trends in long-range corrected functionals due to their increased orbital localization [65–67].

The DFT-calculated HOMO is primarily localized on the $[SbI_5]^{2-}$ inorganic chain, while the LUMO resides on the π* system of the allylimidazolium cation (Figure 8), suggesting an inorganic-to-organic [Sb–I]→π* charge-transfer transition. This spatial separation is similar to what has been reported for related systems such as $(C_7H_7)SbI_4$ [34] and iodido pentelates [68] and supports our interpretation of the experimental UV–Vis absorptions. The electronic structure, thus, reflects limited orbital overlap between chains, consistent with the high optical band gap and low-dimensional character of the material.

Further orbital decomposition shows that lower-lying occupied orbitals (HOMO−1 to HOMO−3) are also localized on the inorganic fragment, while unoccupied orbitals up to LUMO+3 remain predominantly on the organic cation, with the LUMO+2 representing additional imidazole π* contributions (Figure S8).

To contextualize these findings, we also examined the isolated $AImd^+$ cation, whose HOMO is localized on the allyl group and LUMO on the imidazolium ring (Figure S9). This confirms the LUMO acceptor character in the composite system. Although TD-DFT calculations were not performed, the frontier orbital character and DFT-derived HOMO–LUMO gap qualitatively support the charge-transfer assignment and the observed absorption edge. A more quantitative treatment, including TD-DFT and periodic calculations, is ongoing to further refine this analysis.

In the same way, a transition between Br atoms on the $^1{}_\infty[SbBr_5]$ scaffold and the methyl-thiouronium amine moieties of the 1D structure $(CH_3SC(NH_2)_2)_2{}^1{}_\infty[SbBr_5]$ was described [38]. As these and our report are conflicting with the more frequent description of a ligand(iodide)-to-metal(Sb) charge transfer being responsible for the light absorption, with a corresponding iodide-centered conduction band and a Sb-dominated valence band [42,46,48,63,64], we need to carry out more detailed calculations of valence and conduction bands and possible change components in our system, substituting the allylimidazolium and replacing I through Br. Such work is in progress.

To complement the frontier orbital analysis, we calculated global reactivity descriptors (I, A, η, μ, ω) based on Koopmans' and Janak's theorems [69–71] and Pearson's HSAB concept [72]. The electron affinity A remained constant at 3.0 eV across all methods, while PBE0 gave slightly higher ionization energies I (5.9–6.0 eV) and hardness η (0.05–0.06 eV) compared to B3LYP (5.7 eV, 0.05 eV), reflecting modestly increased electronic stability and reduced polarizability. These differences align with the larger HOMO–LUMO gap obtained using PBE0 (3.00 eV vs. experimental 3.15 eV), corroborating its reliability for hybrid metal–halide systems [46,49,73].

It should be noted that our analysis of HOMO–LUMO gaps and reactivity descriptors is intended purely for qualitative comparison of electronic trends among the components. While DFT, especially with effective core potentials like SDD, offers a practical approach for systems containing heavy elements such as Sb and I, it is not designed to yield quantitatively accurate band gaps or excited-state properties, areas that remain under active study. Nonetheless, this strategy reliably captures relative orbital energies and supports our interpretation of charge transfer and general optical behavior in these hybrid systems.

The full set of computed descriptors is provided in the Supplementary Materials (Table S10).

3. Materials and Methods

3.1. Materials

$SbCl_3$ (Sigma-Aldrich, Darmstadt, Germany), hydroiodic acid (57%, Sigma-Aldrich), and 1-allylimidazole (97%, Thermo Fisher Scientific, Hampton, NH, USA) were used without further purification.

3.2. Single Crystal Growth

A solution of $SbCl_3$ in hydroiodic acid (HI) was prepared by slowly dissolving 0.65 g (1 mmol) of $SbCl_3$ in 5 mL of concentrated HI under vigorous stirring, yielding a clear, dark red solution. 1-allylimidazole (0.32 g, 2 mmol) was dissolved in 5 mL of EtOH and combined with 2 mL of concentrated HI. The resulting mixture was added to the $SbCl_3$ solution, producing a clear, dark orange solution. The reaction mixture was heated to 50 °C and stirred for 2 h before filtration. Orange-red lamellar crystals of $(AImd)_2{}^1{}_\infty[SbI_5]$ formed after 3 days of slow evaporation.

3.3. Single-Crystal X-Ray Diffraction

Data were collected at 298(2) K using a Bruker AXS D8 Quest diffractometer (Bruker, Rheinhausen, Germany) equipped with a microfocus sealed tube and a Mo-Kα radiation source (λ = 0.71073 Å). Data reduction was performed using SAINT [74], and a multi-scan absorption correction was applied using SADABS [75]. The structure was solved with Olex2 [76], employing the SHELXT [77] structure solution program via intrinsic phasing, and subsequently refined using the SHELXL [78] refinement package through full-matrix least-squares refinement. All H atoms were positioned geometrically and treated as riding on their parent C and N atoms, with C–H and N–H distances of 0.93/0.97 and 0.86 Å, respectively (Uiso(H) = 1.2 Ueq(C) and Uiso(H) = 1.5 Ueq(N)). Structural details of the refinement and crystallographic parameters are listed in Table S1. CCDC 2432530 contains the supplementary crystallographic data for this paper. These data can be obtained free of charge via www.ccdc.cam.ac.uk/data_request/cif (accessed on 27 May 2025), or by emailing data_request@ccdc.cam.ac.uk, or by contacting The Cambridge Crystallographic Data Centre, 12 Union Road, Cambridge CB2 1EZ, UK; fax: +44 1223 336033. Mercury 4 CSD software was used to illustrate the 3D structure and intermolecular interactions in the crystal packing [79]. The crystal structure was further analyzed using the void and

pore analysis tools included in the Mercury CSD software. The grid spacing was set to 0.3 Å, and the probe size to 1.2 Å. This probe size corresponds to the diameter of the largest sphere that can be inserted without overlapping the framework atoms [80,81].

3.4. Crystal Morphology Simulation

The theoretical crystal morphology of $(AImd)_2{}^1{}_\infty[SbI_5]$ was predicted using the Bravais–Friedel–Donnay–Harker (BFDH) and growth morphology (GM) models within the Morphology module of Materials Studio 7.0 software. The structure was optimized using the Universal Force Field and the Forcite energy method through a geometry optimization procedure. The computations were performed with high precision, yielding a minimum interplanar distance (d_{hkl}) of 1.000 Å, without imposing constraints on the Miller indices (h k l) or the number of generated crystal faces. All calculations were conducted at 0 K, without accounting for surface relaxation. The crystal surfaces were considered as ideal terminations of the bulk structure.

The BFDH model predicts crystal morphology based on lattice symmetry and geometrical parameters, without considering intermolecular interaction energies. It is supported by the observation that stronger intermolecular interactions typically lead to larger interplanar distances (d_{hkl}), which in turn increase the corresponding reciprocal slice energy [82,83].

The GM model, widely used for predicting crystal morphology [84–87], involves the calculation of attachment energies (E_{att}) by accounting for both the crystal symmetry and the nature of intermolecular interactions. It offers a more accurate prediction of crystal habits by evaluating the relative growth rates of individual crystal facets. According to this model, the growth rate of a crystal face is directly proportional to its attachment energy; thus, lower E_{att} values indicate slower-growing crystal faces [55,87].

3.5. Spectroscopy

The FT-IR spectrum was recorded using a Bruker Tensor 27 FT-IR spectrometer (Bruker, Rheinhausen, Germany) in the range of 4000 to 400 cm^{-1}. The Raman spectrum was acquired using a RENISHAW Raman spectrophotometer (Renishaw, Thermo Fisher, Hampton, NH, USA) equipped with a 532 nm laser. UV–Vis diffuse reflectance and absorption spectra were measured on a powder sample mixed with $BaSO_4$ as a reference. The measurements were performed at room temperature using a JASCO V-770 spectrophotometer (Jasco, Tokyo, Japan), covering the wavelength range of 300 to 700 nm.

3.6. Computational Methods

All quantum–chemical calculations were carried out with Gaussian 16 [88] on the crystallographic asymmetric unit, which contains one protonated allylimidazolium cation and one $[SbI_4]^-$ anion. Geometry optimization and harmonic frequency analyses were performed with three hybrid functionals that sample short-, medium-, and long-range exchange: B3LYP [89,90], CAM-B3LYP [91], and PBE0 (keyword PBE1PBE in Gaussian) [92]. Light atoms (C, H, N) were described with the 6-311++G** basis set [93], whereas scalar-relativistic effects on Sb and I were treated with the LANL2DZ and, for comparison, the SDD effective-core potentials [94,95]. Both basis sets have been validated for halogenated and pnictogen-containing systems and provide reliable geometries at reduced computational cost [96,97]. CAM-B3LYP was chosen due to its superior performance in reproducing Sb–I bond lengths in related systems, typically yielding deviations below 0.03 Å from experimental values [98,99].

Alternatively, we also carried out new geometry optimizations using both the mixed-basis set scheme (Sb, I)/(C, N, H) = def2-TZVP/6-311++G** and the uniform def2-TZVPP/def2-TZVPP level (with def2-ECP on Sb and I), combined with CAM-B3LYP and PBE0 functionals. These calculations confirmed that the structural parameters remain

consistent across all tested methods, while the LANL2DZ and SDD basis sets continued to yield HOMO–LUMO gaps most consistent with experiments. The detailed comparison of selected bond lengths, HOMO and LUMO energies, and E_g values is provided in the Supplementary Materials (Table S5) along with the optimized geometries.

Empirical dispersion was included through Grimme's D3 scheme with Becke–Johnson damping to ensure a balanced treatment of non-covalent interactions [100]. All optimizations used an ultrafine integration grid and tight SCF convergence; real vibrational frequencies confirmed that the resulting structures were true minima. Frontier-orbital energies were employed to derive global reactivity indices (HOMO–LUMO gap, electronegativity, hardness, electrophilicity) that clarify charge-transfer tendencies between the cation and anion. These computations provide a consistent, dispersion-corrected picture of the isolated asymmetric unit and underpin the structural and electronic discussions presented below.

The calculations of non-covalent interactions were carried out using Gaussian 16 [88] at the B3LYP-D3/def2-TZVP level of theory [89,101,102]. To evaluate the interactions in the solid-state structure, the crystallographic coordinates were employed, with optimization performed only for the positions of the hydrogen atoms. The interaction energy (ΔE) was calculated as the energy difference between the multicomponent assembly and the sum of the energies of the isolated monomers. These interaction energies were corrected with the Boys and Bernardi counterpoise method for basis set superposition error [103].

The electron density was computed using the Multiwfn program [104] at the same level of theory and used for both quantum theory of atoms in molecules (QTAIM) [105] and NCIplot [106] analyses. Visualization of the results was carried out with the VMD program [107], using the following settings for NCIplot representations: s = 0.3 a.u., ρ cutoff = 0.04 a.u., and color scale range $-0.03 \leq \text{sign}(\lambda_2)\rho \leq 0.03$ a.u.

4. Conclusions

The new one-dimensional, lead-free, hybrid organic–inorganic perovskite material $(AImd)_2{}^1{}_\infty[SbI_5]$ was synthesized and studied using a combination of experimental and computational analyses including crystal morphology prediction, void and pore assessment, spectroscopic characterization, and DFT modeling to approach the structural and optoelectronic properties of the compound. The structure consists of anionic *cis*-zigzag ${}^1{}_\infty[SbI_5]^{2-}$ chains formed through corner-sharing, distorted $[SbI_6]$ octahedra separated by allylimidazolium cations. Non-covalent interaction analysis via QTAIM and NCI revealed the dominant role of coulomb interaction over the C–H···I and N–H···I hydrogen bonding interactions in the supramolecular structure. The growth morphology model accurately reproduces the experimental plate-like habit, with the dominating (0 1 1) facet having a low attachment energy and functional surface chemistry.

The observed band gap of 2.98 eV was well reproduced through DFT calculations using the PBE0 functional. These calculations indicate that a charge transfer from the inorganic ${}^1{}_\infty[SbI_5]^{2-}$ lattice to the π* orbitals of the organic cation is responsible for the low-energy electronic transition ([Sb–I] → π* charge-transfer excitation). This stands in contrast to many reports assigning the absorption in such materials to a ligand-to-metal charge transfer proceeding from iodine 5p states (forming the main contribution of the valence band) to Sb 5p states (dominating the conduction band). This calls for more detailed studies and calculation of valence and conduction bands of the herein presented system with derivatives containing substituted allylimidazolium and replacing I through Br. Such work is in progress.

From the relatively large band gap, we can already now deduce an application for optical filtering, and from the high ionic character with the assumed charge transfer, applications as dielectric material or in photocatalysis seem possible and will be explored in the near future.

Supplementary Materials: The following supporting information can be downloaded at: https://www.mdpi.com/article/10.3390/inorganics13070243/s1. The materials contain Figure S1: Asymmetric unit, SbI_5^{2-} anionic chain, and crystal packing of $(AImd)_2{}^1{}_\infty[SbI_5]$. Figure S2: Perspective view on the crystal structure of $(AImd)_2{}^1{}_\infty[SbI_5]$. Figure S3: Crystal structure of $(AImd)_2{}^1{}_\infty[SbI_5]$ viewed along the crystallographic *c* axis. Figure S4: Crystal structure of $(AImd)_2{}^1{}_\infty[SbI_5]$ viewed along the crystallographic *b* axis. Figure S5: Calculated voids in $(AImd)_2{}^1{}_\infty[SbI_5]$. Figure S6: FT-IR spectrum of $(AImd)_2{}^1{}_\infty[SbI_5]$. Figure S7: Raman spectrum of $(AImd)_2{}^1{}_\infty[SbI_5]$. Figure S8: DFT-calculated molecular orbitals for $(AImd)_2{}^1{}_\infty[SbI_5]$ using the PBE0 functional. Figure S9: DFT-calculated molecular orbitals for $AImd^+$ using the PBE0 functional. Table S1: Selected data for structure solution and refinement of $(AImd)_2{}^1{}_\infty[SbI_5]$. Table S2: Selected experimental bonding parameters for $(AImd)_2{}^1{}_\infty[SbI_5]$. Table S3: Void and pore characteristics of $(AImd)_2{}^1{}_\infty[SbI_5]$. Table S4: Topological parameters obtained from QTAIM analyses, characterizing the hydrogen bonds in the solid-state structure of $(AImd)_2{}^1{}_\infty[SbI_5]$. Table S5: Selected experimental and DFT-calculated equilibrium geometry parameters for $(AImd)_2{}^1{}_\infty[SbI_5]$ and EHOMO, ELUMO and gap Eg energies. Table S6. XYZ coordinates of the DFT-optimized structure of $(AImd)_2{}^1{}_\infty[SbI_5]$ using the CAM-B3LYP functional (Sb, I)/(C, N, H) = def2-TZVP/6-311++G**. Table S7: XYZ coordinates of the DFT-optimized structure of $(AImd)_2{}^1{}_\infty[SbI_5]$ using the CAM-B3LYP functional (Sb, I)/(C, N, H) = def2-TZVPP/def2-TZVPP. Table S8: XYZ coordinates of the DFT-optimized structure of $(AImd)_2{}^1{}_\infty[SbI_5]$ using the PBE0 functional (Sb, I)/(C, N, H) = def2-TZVP/6-311++G**. Table S9: XYZ coordinates of the DFT-optimized structure of $(AImd)_2{}^1{}_\infty[SbI_5]$ using the PBE0 functional (Sb, I)/(C, N, H) = def2-TZVPP/def2-TZVPP. Table S10: DFT-calculated global reactivity descriptors for $(AImd)_2{}^1{}_\infty[SbI_5]$.

Author Contributions: H.F.: Formal analysis, data curation, resources, methodology, funding acquisition, writing—review and editing, writing—original draft. R.B.: Software, methodology, data curation, writing—original draft, data curation. D.M.G.: Software, methodology, data curation, writing—original draft, data curation. A.K.: Supervision, writing—review and editing, writing—original draft. All authors have read and agreed to the published version of the manuscript.

Funding: This work was supported and funded by the Deanship of Scientific Research at Imam Mohammad Ibn Saud Islamic University (IMSIU) (grant number IMSIU-DDRSP2503).

Institutional Review Board Statement: Not applicable.

Informed Consent Statement: Not applicable.

Data Availability Statement: The original contributions presented in this study are included in the article/Supplementary Material. Further inquiries can be directed to the corresponding authors.

Acknowledgments: Imam Mohammad Ibn Saud Islamic University (IMSIU), CONICET-UNT, and University of Cologne are acknowledged for their general support.

Conflicts of Interest: The authors declare no conflicts of interest.

References

1. Zhao, H.; Yang, X.; Bai, Y.; Meng, Q.; Wen, Z.; Sun, H.; Wei, Q.; Huang, D.; Yu, W.W.; Liu, F. Mechanoluminescence from Organic-Inorganic Metal Halide Perovskite Derivative. *Adv. Sci.* **2025**, *12*, e2414588. [CrossRef] [PubMed]
2. Singh, S.; Hamid, Z.; Babu, R.; Gómez-Graña, S.; Hu, X.; McCulloch, I.; Hoye, R.L.Z.; Rao, V.G.; Polavarapu, L. Halide Perovskite Photocatalysts for Clean Fuel Production and Organic Synthesis: Opportunities and Challenges. *Adv. Mater.* **2025**, *2025*, 2419603. [CrossRef] [PubMed]
3. Sheikh, A.D.; Yadav, H.M.; Sharma, K.K.; Shim, J.W.; Lee, J.-J.; Ghanem, M.A. Recent Advances in Innovative Device Designs and Engineering Strategies of Hybrid Perovskite Halides for Efficient Photoelectrochemical and Photocatalytic Applications. *Small* **2025**, *2025*, 2501570. [CrossRef] [PubMed]
4. Berhe, T.A.; Su, W.-N.; Hwang, B.J. Halide Perovskites' Multifunctional Properties: Coordination Engineering, Coordination Chemistry, Electronic Interactions and Energy Applications beyond Photovoltaics. *Inorganics* **2024**, *12*, 182. [CrossRef]
5. Mao, L.; Chen, J.; Vishnoi, P.; Cheetham, A.K. The Renaissance of Functional Hybrid Transition-Metal Halides. *Acc. Mater. Res.* **2022**, *3*, 439–448. [CrossRef]
6. Euvrard, J.; Yan, Y.; Mitzi, D.B. Electrical doping in halide perovskites. *Nat. Rev. Mater.* **2021**, *6*, 531–549. [CrossRef]

7. Guo, X.; Burda, C. Coordination engineering toward high performance organic–inorganic hybrid perovskites. *Coord. Chem. Rev.* **2016**, *320–321*, 53–65. [CrossRef]
8. Saparov, B.; Mitzi, D.B. Organic-Inorganic Perovskites: Structural Versatility for Functional Materials Design. *Chem. Rev.* **2016**, *116*, 4558–4596. [CrossRef]
9. Huang, C.; Gajewiak, E.; Wright, A.; Rodriguez-Kazeem, W.; Heift, D.; Bear, J.C. A comparative meta-analysis of gains in efficiency in Pb and Sn-based perovskite solar cells over the last decade. *Z. Anorg. Allg. Chem.* **2023**, *649*, e202300045. [CrossRef]
10. Nowsherwan, G.A.; Ali, Q.; Ali, U.F.; Ahmad, M.; Khan, M.; Hussain, S.S. Advances in Organic Materials for Next-Generation Optoelectronics: Potential and Challenges. *Organics* **2024**, *5*, 520–560. [CrossRef]
11. Zhou, K.; Qi, B.; Liu, Z.; Wang, X.; Sun, Y.; Zhang, L. Advanced organic–inorganic hybrid materials for optoelectronic applications. *Adv. Funct. Mater.* **2024**, *34*, 2411671. [CrossRef]
12. Morab, S.; Sundaram, M.M.; Pivrikas, A. Review on charge carrier transport in inorganic and organic semiconductors. *Coatings* **2023**, *13*, 1657. [CrossRef]
13. Jonathan, L.; Diguna, L.J.; Samy, O.; Muqoyyanah, M.; Bakar, S.A.; Birowosuto, M.D.; El Moutaouakil, A. Hybrid Organic–Inorganic Perovskite Halide Materials for Photovoltaics towards Their Commercialization. *Polymers* **2022**, *14*, 1059. [CrossRef]
14. Siegler, T.D.; Dawson, A.; Lobaccaro, P.; Ung, D.; Beck, M.E.; Nilsen, G.; Tinker, L.L. The Path to Perovskite Commercialization: A Perspective from the United States Solar Energy Technologies Office. *ACS Energy Lett.* **2022**, *7*, 1728–1734. [CrossRef]
15. Xiang, W.; Liu, S.F.; Tress, W. A review on the stability of inorganic metal halide perovskites: Challenges and opportunities for stable solar cells. *Energy Environ. Sci.* **2021**, *14*, 2090–2113. [CrossRef]
16. Zhuang, J.; Wang, J.; Yan, F. Review on Chemical Stability of Lead Halide Perovskite Solar Cells. *Nano-Micro Lett.* **2023**, *15*, 84. [CrossRef] [PubMed]
17. Sakhatskyi, K.; John, R.A.; Guerrero, A.; Tsarev, S.; Sabisch, S.; Das, T.; Matt, G.J.; Yakunin, S.; Cherniukh, I.; Kotyrba, M.; et al. Assessing the Drawbacks and Benefits of Ion Migration in Lead Halide Perovskites. *ACS Energy Lett.* **2022**, *7*, 3401–3414. [CrossRef] [PubMed]
18. Ahmed, S.; Gondal, M.A.; Alzahrani, A.S.; Parvaz, M.; Ahmed, A.; Hussain, S. Recent Trends and Challenges in Lead-Free Perovskite Solar Cells: A Critical Review. *ACS Appl. Energy Mater.* **2024**, *7*, 1382–1397. [CrossRef]
19. Yao, J.-Y.; Liu, H.; Chen, Z.-N.; Ma, B.; Xu, L.-J. Low-Dimensional Lead-Free Metal Halides for Efficient Electrically Driven Light-Emitting Diodes. *Angew. Chem. Int. Ed.* **2025**, *64*, e202423185. [CrossRef] [PubMed]
20. EU Phasing Out Use of Pb. Available online: https://echa.europa.eu/hot-topics/lead (accessed on 27 May 2025).
21. Li, Y.J.; Mu, B.H.; Li, H.B.; Tang, S.C.; Tian, J.; Li, Y.; Ji, Z.Y.; Wang, Y.J.; He, T.; Emeline, A.V.; et al. Bi-Based Metal Halide Perovskites and Their Photocatalytic Properties: A Review. *Energy Fuels* **2025**, *39*, 2986–3007. [CrossRef]
22. Wang, X.; Hu, B.; Li, Y.; Zhang, G. Lead-Free Halide Perovskite Photocatalysts for Photocatalytic CO_2 Reduction: A Review. *Sol. RRL* **2023**, *7*, 2300410. [CrossRef]
23. Chen, X.; Jia, M.; Xu, W.; Pan, G.; Zhu, J.; Tian, Y.; Wu, D.; Li, X.; Shi, Z. Recent Progress and Challenges of Bismuth-Based Halide Perovskites for Emerging Optoelectronic Applications. *Adv. Optical Mater.* **2023**, *11*, 2202153. [CrossRef]
24. Coccia, C.; Moroni, M.; Malavasi, L. Chiral Metal Halide Perovskites: Focus on Lead-Free Materials and Structure-Property Correlations. *Molecules* **2023**, *28*, 6166. [CrossRef] [PubMed]
25. Priyadarshini, P.; Senapati, S.; Naik, R. Lead-free organic inorganic hybrid halide perovskites: An emerging candidate for bifunctional applications. *Ren. Sust. Energy Rev.* **2023**, *186*, 113649. [CrossRef]
26. Jin, Z.; Zhang, Z.; Xiu, J.; Song, H.; Gatti, T.; He, Z. A critical review on bismuth and antimony halide based perovskites and their derivatives for photovoltaic applications: Recent advances and challenges. *J. Mater. Chem. A* **2020**, *8*, 16166–16188. [CrossRef]
27. Hu, Y.-Q.; Hui, H.-Y.; Lin, W.-Q.; Wen, H.-Q.; Yang, D.-S.; Feng, G.-D. Crystal and Band-Gap Engineering of One-Dimensional Antimony/Bismuth-Based Organic−Inorganic Hybrids. *Inorg. Chem.* **2019**, *58*, 16346–16353. [CrossRef]
28. Ganose, A.M.; Savory, C.N.; Scanlon, D.O. Beyond methylammonium lead iodide: Prospects for the emergent field on ns^2 containing solar absorbers. *Chem. Commun.* **2017**, *53*, 20–44. [CrossRef]
29. Jin, J.-C.; Shen, N.-N.; Wang, Z.-P.; Peng, Y.-C.; Huang, X.-Y. Photoluminescent ionic metal halides based on s^2 typed ions and aprotic ionic liquid cations. *Coord. Chem. Rev.* **2021**, *448*, 214185. [CrossRef]
30. Rowinska, M.; Stefanska, D.; Bednarchuk, T.J.; Zareba, J.K.; Jakubas, R.; Gagor, A. Polymorphism and Red Photoluminescence Emission from $5s^2$ Electron Pairs of Sb(III) in a New One-Dimensional Organic–Inorganic Hybrid Based on Methylhydrazine: MHy_2SbI_5. *Molecules* **2024**, *29*, 455. [CrossRef]
31. Yao, L.; Xue, K.-H.; Tong, H.; Chen, C.; Niu, G.; Yang, W.; Tang, J. Dimensional Control of Chiral Antimony Halide Compounds for Enhanced Circular Dichroism. *Cryst. Growth Des.* **2022**, *22*, 5552–5558. [CrossRef]
32. Wang, Z.; Zhang, Z.; Sung, H.H.; Williams, I.D.; Lu, H. Structural Asymmetry and Chiroptical Activity of Chiral Antimony-Halide Hybrids. *Eur. J. Inorg. Chem.* **2022**, *2022*, e202200275. [CrossRef]

33. Liu, K.; Deng, C.; Li, C.; Zhang, X.; Cao, J.; Yao, J.; Zhao, J.; Jiang, X.; Lin, Z.; Liu, Q. Hybrid Metal-Halide Infrared Nonlinear Optical Crystals of (TMEDA)MI_5 (M = Sb, Bi) with High Stability. *Adv. Opt. Mater.* **2021**, *9*, 2101333. [CrossRef]
34. Oswald, I.W.; Mozur, E.M.; Moseley, I.P.; Ahn, H.; Neilson, J.R. Hybrid Charge-Transfer Semiconductors:$(C_7H_7)SbI_4$, $(C_7H_7)BiI_4$, and Their Halide Congeners. *Inorg. Chem.* **2019**, *58*, 5818–5826. [CrossRef] [PubMed]
35. Gao, J.X.; Hua, X.N.; Chen, X.G.; Mei, G.Q.; Liao, W.Q. $[C_6N_2H_{18}][SbI_5]$: A Lead-free Hybrid Halide Semiconductor with Exceptional Dielectric Relaxation. *Inorg. Chem.* **2019**, *58*, 4337–4343. [CrossRef]
36. Parmar, S.; Pal, S.; Biswas, A.; Gosavi, S.; Chakraborty, S.; Reddy, M.C.; Ogale, S. Designing a new family of oxonium-cation based structurally diverse organic-inorganic hybrid iodoantimonate crystals. *Chem. Commun.* **2019**, *55*, 7562–7565. [CrossRef]
37. Dennington, A.J.; Weller, M.T. Synthesis, structure and optoelectronic properties of hybrid iodobismuthate & iodoantimonate semiconducting materials. *Dalton Trans.* **2018**, *47*, 3469–3484. [CrossRef]
38. Mousdis, G.A.; Ganotopoulos, N.M.; Barkaoui, H.; Abid, Y.; Psycharis, V.; Savvidou, A.; Raptopoulou, C.P. One-Dimensional Organic–Inorganic Hybrid Materials Based on Antimony. *Eur. J. Inorg. Chem.* **2017**, *2017*, 3401–3408. [CrossRef]
39. Qi, S.; Cheng, P.; Han, X.; Ge, F.; Shi, R.; Xu, L.; Li, G.; Xu, J. Organic–inorganic hybrid antimony(III) halides for second harmonic generation. *Cryst. Growth Des.* **2022**, *22*, 6545–6553. [CrossRef]
40. Li, Z.; Li, Y.; Liang, P.; Zhou, T.; Wang, L.; Xie, R.-J. Dual-band luminescent lead-free antimony chloride halides with near-unity photoluminescence quantum efficiency. *Chem. Mater.* **2019**, *31*, 9363–9371. [CrossRef]
41. Jridi, C.; Elleuch, N.; Shova, S.; Boujelbene, M. New lead-free Iodoantimonatehalide semiconductor: Synthesis, Structural characterization, DFT calculations, Hirshfeld surface, Thermal behavior, vibrational and optical properties. *J. Mol. Struct.* **2025**, *1321*, 139781. [CrossRef]
42. Shestimerova, T.A.; Medved'ko, A.V.; Bykov, M.A.; Kalinin, M.A.; Metlin, M.T.; Taydakov, I.V.; Gontcharenko, V.E.; Wei, Z.; Dikarev, E.V.; Vatsadze, S.Z.; et al. A new supramolecular tecton: The crucial impact of the polycation charge and geometry of H-bonds on the structure and properties of halometallates in the solid state. *Dalton Trans.* **2025**, *54*, 6983–6992. [CrossRef] [PubMed]
43. Chen, D.; Song, Z.; Yang, C.; Wei, Y.; Liu, G.; Meng, L.; Wu, Q.; Dang, Y. Nonlinear Optical Effects of Hybrid Antimony(III) Halides Induced by Stereoactive $5s^2$ Lone Pairs and Trimethylammonium Cations. *Inorg. Chem.* **2024**, *63*, 10304–10311. [CrossRef] [PubMed]
44. Zeng, Z.; Zhang, G.; Wang, Y.; Zhang, M.; Tian, L.; Cheng, Z.; Lian, H.; Lin, J. Gradient Luminescence Enhancement in Organic Metal Halide Perovskites via the Suppression of $[SbCl_n]_{3-n}$ Unit Distortion. *Inorg. Chem.* **2024**, *63*, 24331–24341. [CrossRef] [PubMed]
45. Hou, A.; Fan, L.; Xiong, Y.; Lin, J.; Liu, K.; Chen, M.; Guo, Z.; Zhao, J.; Liu, Q. Zero-Dimensional Halides with ns^2 Electron (Sb^{3+}) Activation to Generate Broad Photoluminescence. *Inorg. Chem.* **2023**, *62*, 12501–12509. [CrossRef]
46. Rowinska, M.; Piecha-Bisiorek, A.; Medycki, W.; Durlak, P.; Jakubas, R.; Gagor, A. Structural, Electric and Dynamic Properties of $(Pyrrolidinium)_3[Bi_2I_9]$ and $(Pyrrolidinium)_3[Sb_2I_9]$: New Lead-Free, Organic-Inorganic Hybrids with Narrow Band Gaps. *Molecules* **2023**, *28*, 3894. [CrossRef]
47. Luo, J.B.; Wei, J.H.; Zhang, Z.Z.; Kuang, D.B. Water-Molecule-Induced Emission Transformation of Zero-Dimension Antimony-Based Metal Halide. *Inorg. Chem.* **2022**, *61*, 338–345. [CrossRef]
48. Szklarz, P.; Jakubas, R.; Medycki, W.; Gagor, A.; Cichos, J.; Karbowiak, M.; Bator, G. $(C_3N_2H_5)_3Sb_2I_9$ and $(C_3N_2H_5)_3Bi_2I_9$: Ferroelastic lead-free hybrid perovskite-like materials as potential semiconducting absorbers. *Dalton Trans.* **2022**, *51*, 1850–1860. [CrossRef]
49. Wu, Y.; Xiang, G.; Zhang, M.; Wei, D.; Cheng, C.; Leng, J.; Ma, H. Electronic Structures and Photoelectric Properties in $Cs_3Sb_2X_9$ (X = Cl, Br, or I) under High Pressure: A First Principles Study. *Nanomaterials* **2022**, *12*, 2982. [CrossRef]
50. Li, Y.; Xu, Z.; Liu, X.; Tao, K.; Han, S.; Wang, Y.; Liu, Y.; Li, M.; Luo, J.; Sun, Z. Two Heteromorphic Crystals of Antimony-Based Hybrids Showing Tunable Optical Band Gaps and Distinct Photoelectric Responses. *Inorg. Chem.* **2019**, *58*, 6544–6549. [CrossRef]
51. Cheng, J.; Qian, P.; Yang, M.; Huang, L.; Zeng, H.; Zou, G.; Lin, Z. Second-Harmonic Generation in Homochiral Antimony Halides Directed by *L*-Histidine. *Inorg. Chem.* **2023**, *62*, 16673–16676. [CrossRef]
52. Gilday, L.C.; Robinson, S.W.; Barendt, T.A.; Langton, M.J.; Mullaney, B.R.; Beer, P.D. Halogen Bonding in Supramolecular Chemistry. *Chem. Rev.* **2015**, *115*, 7118–7195. [CrossRef] [PubMed]
53. Ferjani, H.; Chebbi, H.; Fettouhi, M. One-Dimensional Organic–Inorganic Material $(C_6H_9N_2)_2BiCl_5$: From Synthesis to Structural, Spectroscopic, and Electronic Characterizations. *Int. J. Mol. Sci.* **2021**, *22*, 2030. [CrossRef] [PubMed]
54. Ferjani, H.; Lemine, O.; Ben Smida, Y.; Salah, N.; Kaouach, H.; Saadi, F.; Wahbi, H.I.; Almashnowi, M.Y.; Ramadan, R.; Onwudiwe, D.C. Visible emission from a zero-dimensional tin-based organic-inorganic metal halide for luminescent devices: Experimental and theoretical investigation. *J. Mol. Struct.* **2025**, *1327*, 141210. [CrossRef]
55. Ferjani, H. Structural, Hirshfeld surface analysis, morphological approach, and spectroscopic study of new hybrid iodobismuthate containing tetranuclear 0D cluster $Bi_4I_{16}{\cdot}4(C_6H_9N_2)$ $2(H_2O)$. *Crystals* **2020**, *10*, 397. [CrossRef]
56. Robinson, K.; Gibbs, G.V.; Ribbe, P.H. Quadratic elongation: A quantitative measure of distortion in coordination polyhedra. *Science* **1971**, *172*, 567–570. [CrossRef]
57. Jiang, X.; Li, M.; Tao, Y.; Zhang, M.; Li, X.; Zhang, T.; Gu, J.; Bai, G.; Zheng, N.; Zhao, X.; et al. One-dimensional lead halide perovskite quantum ribbons with controllable edge terminations and ribbon widths. *Chem* **2025**, *11*, 102548. [CrossRef]

58. Espinosa, E.; Molins, E.; Lecomte, C. Hydrogen bond strengths revealed by topological analyses of experimentally observed electron densities. *Chem. Phys. Lett.* **1998**, *285*, 170–173. [CrossRef]
59. Zaib, S.; Khan, I.; Ibrar, A.; McAdam, C.J.; Abdou, S.N.; Ibrahim, M.M.; El-Bahy, S.M.; Frontera, A. Energetic Features of H-Bonded and Antiparallel π-Stacked Supramolecular Assemblies in Pyrazolones: Experimental, Computational and Biological Analyses. *J. Mol. Struct.* **2025**, *1318*, 139232. [CrossRef]
60. Rocha, M.; Saeed, A.; Gil, D.M.; Echeverría, G.A.; Piro, O.E.; Khurshid, A.; Arshad, M.; Ali Shah, S.A.; Erben, M.F. Crystal Engineering with Novel Antipyride Derivatives: Insights from X-ray Diffraction, Hirshfeld Surface Analysis, and DFT Calculations on Intermolecular Interactions. *J. Mol. Struct.* **2025**, *1319*, 139450. [CrossRef]
61. Woensdregt, C.F. Hartman-Perdok Theory: Influence of Crystal Structure and Crystalline Interface on Crystal Growth. *Faraday Discuss.* **1993**, *95*, 97–107. [CrossRef]
62. Klein, J.; Kampermann, L.; Mockenhaupt, B.; Behrens, M.; Strunk, J.; Bacher, G. Limitations of the Tauc Plot Method. *Adv. Funct. Mater.* **2023**, *33*, 2304523. [CrossRef]
63. Lin, F.; Yang, C.; Chen, R.; Wei, W.; Liu, M.; Wang, J.; Guo, F. Near-Unity Emission in Zero-Dimensional Sb(III)-Based Halides Intervened by Hydrogen Bonds towards Efficient Solid-State Lighting Technology. *J. Alloys Compd.* **2024**, *976*, 173054. [CrossRef]
64. Li, W.; Wang, Y.; Yin, H.; Chen, J.; Han, K.; Liu, F.; Zhang, R. Excitation-Dependent Emission in Sb^{3+}-Doped All-Inorganic Rare-Earth Double Perovskites for Anticounterfeiting Applications. *Inorg. Chem.* **2024**, *63*, 10481–10489. [CrossRef] [PubMed]
65. Lee, J.; Rettig, A.; Feng, X.; Epifanovsky, E.; Head-Gordon, M. Faster Exact Exchange for Solids via occ-RI-K: Application to Combinatorially Optimized Range-Separated Hybrid Functionals for Simple Solids with Pseudopotentials Near the Basis Set Limit. *J. Chem. Theory Comput.* **2022**, *18*, 7336–7349. [CrossRef] [PubMed]
66. Baer, R.; Livshits, E.; Salzner, U. Tuned Range-Separated Hybrids in Density Functional Theory. *Annu. Rev. Phys. Chem.* **2010**, *12*, 85–109. [CrossRef] [PubMed]
67. Li, C.; Zheng, X.; Qiang Su, N.; Yang, W. Localized orbital scaling correction for systematic elimination of delocalization error in density functional approximations. *Natl. Sci. Rev.* **2018**, *5*, 203–215. [CrossRef]
68. Möbs, J.; Stuhrmann, G.; Wippermann, S.; Heine, J. Optical Properties and Metal-Dependent Charge Transfer in Iodido Pentelates. *ChemPlusChem* **2023**, *88*, e202200403. [CrossRef]
69. Koopmans, T. Über die Zuordnung von Wellenfunktionen und Eigenwerten zu den Einzelnen Elektronen Eines Atoms. *Physica* **1934**, *1*, 104–113. [CrossRef]
70. Janak, J.F. Proof that ∂E/∂ni = ε in density-functional theory. *Phys. Rev. B* **1978**, *18*, 7165–7168. [CrossRef]
71. Tsuneda, T.; Song, J.-W.; Suzuki, S.; Hirao, K. On Koopmans' theorem in density functional theory. *J. Chem. Phys.* **2010**, *133*, 174101. [CrossRef]
72. Pearson, R.G. Absolute electronegativity and hardness: Application to inorganic chemistry. *Inorg. Chem.* **1988**, *27*, 734–740. [CrossRef]
73. Wang, H.; Tal, A.; Bischoff, T.; Gono, P.; Pasquarello, A. Accurate and efficient band-gap predictions for metal halide perovskites at finite temperature. *npj Comput. Mater.* **2022**, *8*, 237. [CrossRef]
74. Bruker AXS. *SAINT Software Reference Manual*; Bruker AXS Inc.: Madison, WI, USA, 1998.
75. Sheldrick, G. *SADABS*; Bruker Axs Inc.: Madison, WI, USA, 2007.
76. Dolomanov, O.V.; Bourhis, L.J.; Gildea, R.J.; Howard, J.A.; Puschmann, H. OLEX2: A complete structure solution, refinement and analysis program. *Appl. Crystallogr.* **2009**, *42*, 339–341. [CrossRef]
77. Sheldrick, G.M. SHELXT–Integrated space-group and crystal-structure determination. *Acta Crystallogr. C Found. Crystallogr.* **2015**, *71*, 3–8. [CrossRef]
78. Sheldrick, G.M. Crystal structure refinement with SHELXL. *Acta Crystallogr. C Struct. Chem.* **2015**, *71*, 3–8. [CrossRef] [PubMed]
79. Macrae, C.F.; Sovago, I.; Cottrell, S.J.; Galek, P.T.A.; McCabe, P.; Pidcock, E.; Platings, M.; Shields, G.P.; Stevens, J.S.; Towler, M.; et al. Mercury 4.0: From visualization to analysis, design and prediction. *J. Appl. Crystallogr.* **2020**, *53*, 226–235. [CrossRef]
80. Hobday, C.L.; Woodall, C.H.; Lennox, M.J.; Frost, M.; Kamenev, K.; Duren, T.; Morrison, C.A.; Moggach, S.A. Understanding the adsorption process in ZIF-8 using high pressure crystallography and computational modelling. *Nat. Commun.* **2018**, *9*, 1429. [CrossRef]
81. Brekalo, I.; Lisac, K.; Ramirez, J.R.; Pongrac, P.; Xu, Y.; Ferguson, M.; Marrett, J.M.; Arhangelskis, M.; Friščić, T.; Holman, K.T. Mechanochemical Solid Form Screening of Zeolitic Imidazolate Frameworks using Structure-Directing Liquid Additives. *ChemRxiv* **2025**. [CrossRef]
82. Gao, Y.; Song, W.; Yang, J.; Ji, X.; Wang, N.; Huang, X.; Wang, T.; Hao, H. Crystal Morphology Prediction Models and Regulating Methods. *Crystals* **2024**, *14*, 484. [CrossRef]
83. Donnay, J.D.H.; Harker, D. A new law of crystal morphology extending the law of Bravais. *Amer Mineral. J. Earth Planet. Mater.* **1937**, *22*, 446–467.
84. Ferjani, H. Novel flucytosine salt: Structure, Hirshfeld surface analysis, morphology, FIMs, and computational studies. *J. Mol. Graph. Model.* **2025**, *137*, 109012. [CrossRef]

85. Gasteiger, J.; Marsili, M. A new model for calculating atomic charges in molecules. *Tetrahedron Lett.* **1978**, *19*, 3181–3184. [CrossRef]
86. Hartman, P.; Bennema, P. The attachment energy as a habit controlling factor: I. Theoretical considerations. *J. Cryst. Growth* **1980**, *49*, 145–156. [CrossRef]
87. Hartman, P. The attachment energy as a habit controlling factor: III. Application to corundum. *J. Cryst. Growth* **1980**, *49*, 166–170. [CrossRef]
88. Frisch, M.J.; Trucks, G.W.; Schlegel, H.B.; Scuseria, G.E.; Robb, M.A.; Cheeseman, J.R.; Scalmani, G.; Barone, V.; Petersson, G.A.; Nakatsuji, H.; et al. *Gaussian 16 Rev. C.01*; Gaussian, Inc.: Wallingford, CT, USA, 2016.
89. Becke, A.D. Density-functional thermochemistry. III. The role of exact exchange. *J. Chem. Phys.* **1993**, *98*, 5648–5652. [CrossRef]
90. Lee, C.; Yang, W.; Parr, R.G. Development of the Colle-Salvetti correlation-energy formula into a functional of the electron density. *Phys. Rev. B Condens. Matter* **1988**, *37*, 785–789. [CrossRef]
91. Chai, J.D.; Head-Gordon, M. Long-range corrected hybrid density functionals with damped atom-atom dispersion corrections. *Phys. Chem. Chem. Phys.* **2008**, *10*, 6615–6620. [CrossRef]
92. Adamo, C.; Barone, V. Toward reliable density functional methods without adjustable parameters: The PBE0 model. *J. Chem. Phys.* **1999**, *110*, 6158–6170. [CrossRef]
93. Clark, T.; Chandrasekhar, J.; Spitznagel, G.W.; Schleyer, P.V.R. Efficient diffuse function-augmented basis sets for anion calculations. III. The 3-21+ G basis set for first-row elements, Li–F. *J. Comput. Chem.* **1983**, *4*, 294–301. [CrossRef]
94. Hay, P.J.; Wadt, W.R. Ab initio effective core potentials for molecular calculations. Potentials for the transition metal atoms Sc to Hg. *J. Chem. Phys.* **1985**, *82*, 270–283. [CrossRef]
95. Andrae, D.; Häußermann, U.; Dolg, M.; Stoll, H.; Preuss, H. Energy-adjusted ab initio pseudopotentials for the second and third row transition elements. *Theor. Chim. Acta* **1990**, *77*, 123–141. [CrossRef]
96. Cundari, T.R.; Stevens, W.J. Effective core potential methods for the lanthanides. *J. Chem. Phys.* **1993**, *98*, 5555–5565. [CrossRef]
97. Dolg, M.; Stoll, H.; Preuss, H. A combination of quasirelativistic pseudopotential and ligand field calculations for lanthanoid compounds. *Theor. Chim. Acta* **1993**, *85*, 441–450. [CrossRef]
98. Li, M.; Reimers, J.R.; Ford, M.J.; Kobayashi, R.; Amos, R.D. Accurate prediction of the properties of materials using the CAM-B3LYP Density Functional. *J. Comput. Chem.* **2021**, *42*, 1486–1497. [CrossRef]
99. Kodikara, M.S.; Stranger, R.; Humphrey, M.G. Long-Range Corrected DFT Calculations of First Hyperpolarizabilities and Excitation Energies of Metal Alkynyl Complexes. *ChemPhysChem* **2018**, *19*, 1537–1546. [CrossRef]
100. Grimme, S.; Ehrlich, S.; Goerigk, L. Effect of the damping function in dispersion corrected density functional theory. *J. Comput. Chem.* **2011**, *32*, 1456–1465. [CrossRef]
101. Grimme, S.; Antony, J.; Ehrlich, S.; Krieg, H. A consistent and accurate ab initio parametrization of density functional dispersion correction (DFT-D) for the 94 elements H-Pu. *J. Chem. Phys.* **2010**, *132*, 154104. [CrossRef]
102. Weigend, F.; Ahlrichs, R. Balanced basis sets of split valence, triple zeta valence and quadruple zeta valence quality for H to Rn: Design and assessment of accuracy. *Phys. Chem. Chem. Phys.* **2005**, *7*, 3297–3305. [CrossRef]
103. Boys, S.F.; Bernardi, F. The calculation of small molecular interactions by the differences of separate total energies. Some procedures with reduced errors. *Mol. Phys.* **1970**, *19*, 553–556. [CrossRef]
104. Lu, T.; Chen, F. Multiwfn: A multifunctional wavefunction analyzer. *J. Comput. Chem.* **2012**, *33*, 580–592. [CrossRef]
105. Bader, R.F. A bond path: A universal indicator of bonded interactions. *J. Phys. Chem. A* **1998**, *102*, 7314–7323. [CrossRef]
106. Contreras-Garcia, J.; Johnson, E.R.; Keinan, S.; Chaudret, R.; Piquemal, J.P.; Beratan, D.N.; Yang, W. NCIPLOT: A program for plotting non-covalent interaction regions. *J. Chem. Theory Comput.* **2011**, *7*, 625–632. [CrossRef]
107. Humphrey, W.; Dalke, A.; Schulten, K. VMD: Visual molecular dynamics. *J. Mol. Graph.* **1996**, *14*, 33–38. [CrossRef]